Inorganic Chemistry

pubs.acs.org/IC

Article

Unravelling Magneto-Structural Correlations in Pseudo $D_{5h/6h}$-Symmetric Dy(III) Single-Molecule Magnets

Tanu Sharma* and Gopalan Rajaraman*

Cite This: *Inorg. Chem.* 2025, 64, 24506−24516

Read Online

ACCESS | Metrics & More | Article Recommendations | Supporting Information

ABSTRACT: Recent breakthroughs in Dy^{III}-based single-molecule magnets (SMMs), including magnetic hysteresis at liquid nitrogen temperatures, have significantly advanced their potential for real-world applications. However, challenges persist, especially in achieving precise geometric control over magnetic anisotropy and developing air-stable SMMs with higher blocking temperatures (T_B). While ab initio multireference methods such as CASSCF/RASSI-SO have provided valuable insights into individual systems, these findings are often system-specific and difficult to generalize. In this work, we address this limitation by combining DFT and ab initio CASSCF/RASSI-SO calculations with systematic correlation analysis across a diverse set of pseudo-D_{5h} and D_{6h} Dy^{III} complexes. These systems incorporate a variety of axial ligands (F^-, *t*-BuO^-, MeOH, Cp^-, $OCNH_2$, corannulene) and equatorial donors (nitrogen/oxygen/sulfur-donor 15-crown-5 and 18-crown-6), including mixed-ligand architectures. Our analysis uncovers strong trends linking high energy barriers (U_{cal} > 1200 cm^{-1}) to three key geometric factors: minimal Dy displacement (<0.1 Å) from the equatorial plane, low angular distortion (<2°), and a high axial ratio (>0.90). These correlations, observed across multiple complexes, provide a set of generalizable design principles for engineering high-performance Dy^{III} SMMs in pseudo- pseudo-D_{5h} and D_{6h} geometries, laying the groundwork for the next generation of air-stable, high-blocking-temperature SMMs.

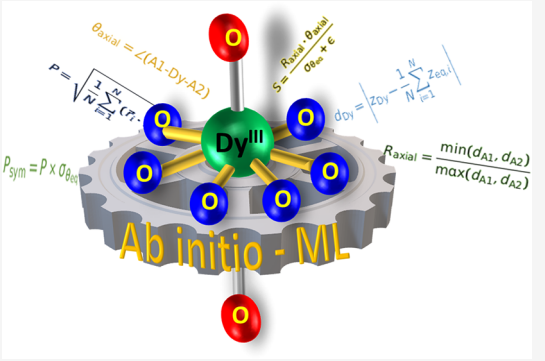

1. INTRODUCTION

Single-molecule magnets (SMMs) have gained significant attention due to their potential applications in high-density memory storage, spintronics, molecular qubits, and multiferroic materials.[1] Among the various types of SMMs, mononuclear lanthanide-based systems have emerged as promising candidates for achieving high blocking temperatures (T_B) and large energy barriers for magnetization reversal (U_{eff}).[2] The Dysprosium complexes, in particular, have been widely studied due to their large total angular momentum (J = 15/2) and strong axial anisotropy, making them ideal for realizing high-performance SMMs. However, despite numerous advances, the realization of robust and high-T_B lanthanide SMMs under ambient conditions remains a formidable challenge.[2,3]

Recent developments in dysprosium metallocene-based magnets have demonstrated the feasibility of achieving blocking temperatures beyond liquid nitrogen temperatures.[3c,e] However, these systems suffer from instability under ambient conditions, limiting their practical applications.[3c,e] Previous theoretical studies have shown that linear two-coordinate Dy^{III} complexes could exhibit relaxation through the highest excited state, leading to enhanced performance.[4] Nevertheless, such low-coordinate Dy^{III} systems are inherently unstable. One approach to overcoming this limitation is through encapsulation within fullerene cages, which provide a stable environment while preserving the axial ligand field.[5] Experimental validation of theoretical predictions has confirmed the efficacy of lanthanide-encapsulated fullerenes as promising SMM candidates, with remarkable energy barriers and high relaxation times.[5a,e,6] However, the synthetic challenges and low yields associated with these materials make their widespread use impractical.[7]

To circumvent these issues, alternative ligand scaffolds capable of promoting axiality while offering greater stability and synthetic accessibility are highly desirable. Corannulene-based ligands, with their bowl-shaped structure and 5-fold symmetry reminiscent of C_{60} fragments, offer a promising route.[8] Encouraged by their coordination chemistry with transition metals, theoretical investigations have explored their viability in stabilizing lanthanide-based SMMs.[9,10] Complementary to this, crown ether ligands have also gained attention for their ability to modulate equatorial ligand fields. Weakening the equatorial field while retaining strong axial interactions is critical for enhancing the SMM properties of Dy^{I33II} complexes.[11] Crown ethers allow precise control over donor

Received: August 21, 2025
Revised: November 8, 2025
Accepted: November 26, 2025
Published: December 11, 2025

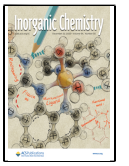

Scheme 1. Schematic Representation of Dy^{III} SMM Models Studied in This Work and in Selected Studies by Other Groups

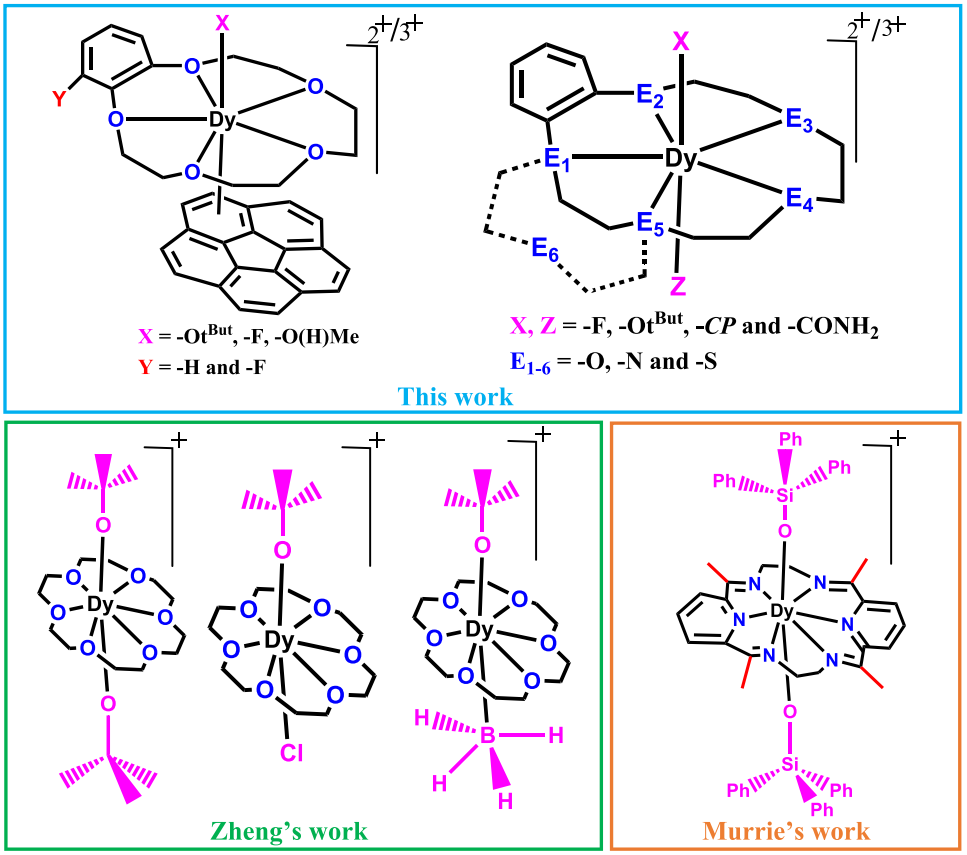

atom positioning and coordination environment, making them ideal platforms for systematic tuning of magnetic anisotropy.

Notably, recent work has shown that Dy^{III} complexes incorporating 18-crown-6 ligands and axial tert-butoxide donors can exhibit exceptional SMM performance. The complex $[Dy(18\text{-}C\text{-}6)(t\text{-}BuO)_2][I_3]$[11c] displays an impressive U_{eff} of 1634 cm^{-1} and a T_B of 10 K under zero external field. This result underscores the high axiality achievable through judicious tuning of axial and equatorial coordination environments using crown ethers. Complementing this, the complex $[Dy(BH_4)_2(18\text{-}C\text{-}6)][Na(THF)_2(18\text{-}C\text{-}6)][BPh_4]_2$,[11e] which also features an 18-crown-6 equatorial coordination, with a U_{eff} of 87 cm^{-1}. These studies collectively highlight the versatility of crown ether ligands in creating a tunable and anisotropic coordination sphere that supports slow magnetic relaxation. Motivated by these findings and the inherent structural adaptability of crown ethers, we pursued a theoretical screening of crown ether–based Dy^{III} complexes to better understand the geometry–anisotropy relationship and identify promising candidates for next-generation SMMs.

In parallel with experimental efforts, theoretical methodologies—particularly those based on multireference ab initio approaches such as CASSCF/SINGLE_ANISO, have been instrumental in advancing the understanding and design of Dy^{III}-based SMMs. These tools allow accurate prediction of magnetic anisotropy, relaxation barriers, and g-tensors, providing critical guidance in molecular design. More recently, the development of spin-phonon coupling models has offered deeper insight into the mechanisms of magnetic relaxation, highlighting vibrational modes that critically influence SMM performance. While the U_{cal} model offers useful first-order insights into magnetic anisotropy, it does not account for dynamic relaxation pathways that ultimately govern magnetic blocking. In this regard, spin–phonon coupling models and ab initio spin dynamics approaches offer a more complete and predictive framework for understanding and designing high-performance lanthanide-based SMMs.[12]

While the concept of maximizing axial ligand field strength and minimizing equatorial interactions is well-established, additional factors, such as the nature of donor atoms, their number and arrangement in axial/equatorial positions, and the overall planarity of the equatorial ligand field, also play pivotal roles. These subtle yet significant structural contributions can either reinforce or compromise magnetic performance. While recent advances in data-driven approaches have begun to influence chemical research, comprehensive models that disentangle and prioritize the interplay of structural and electronic factors in SMMs are still relatively limited.[13] The potential of combining high-level theoretical data (e.g., from CASSCF) with geometric descriptors to rationalize and predict SMM behavior remains an emerging area of interest.[14] Such strategies could, in time, offer complementary pathways to conventional design, enabling more informed screening of candidate molecules. In this study, we systematically examine 20 complexes incorporating corannulene and crown-ether ligands, using a structure–property analysis framework to uncover geometric factors that most significantly influence the magnetic behavior of Dy^{III}-based SMMs. By correlating key structural parameters with computed energy barriers, we aim to establish practical design principles for enhancing SMM performance within this molecular class.

https://doi.org/10.1021/acs.inorgchem.5c03903
Inorg. Chem. 2025, 64, 24506−24516

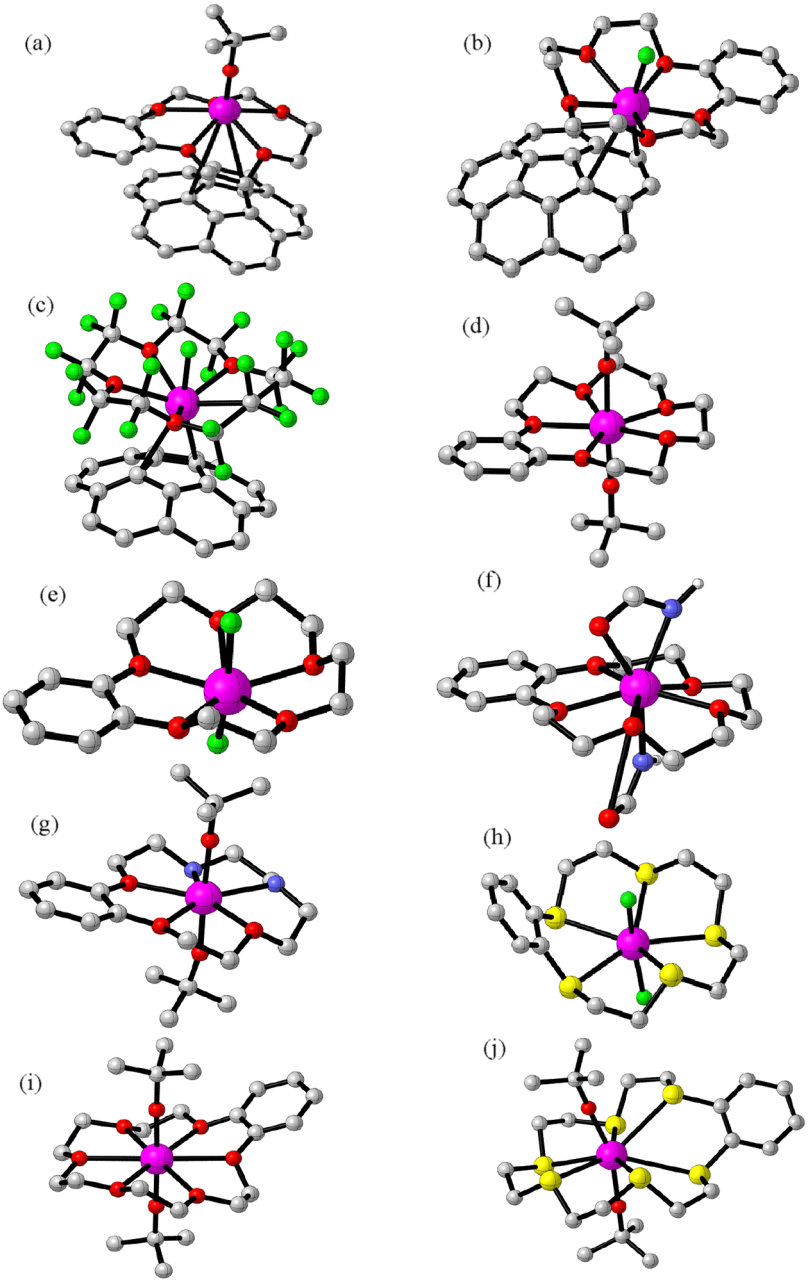

Figure 1. Geometries of various models employed (a) **2**, (b) **4**, (c) **9**, (d) **10**, (e) **12**, (f) **15**, (g) **16**, (h) **18**, (i) **19** and (j) **20**. Color code: Dy^{III} = pink, C = light gray, O = red, *F* = green, S = light yellow and *N* = blue. Here, all the hydrogens are omitted for clarity.

This set includes computational analysis to explore the impact of axial ligands in conjunction with the equatorial frameworks. Corannulene-functionalized Dy^{III} complexes have been studied in combination with different axial ligands such as fluoro, methoxy, and *Cp*-based groups. Similarly, crown ether-based Dy^{III} complexes with varying axial ligands, including $OC(CH_3)_3$, *Cp*, and F^-, have been evaluated for their effects on magnetic anisotropy and relaxation mechanisms (see Scheme 1 and Figure S3). Here we have undertaken studies 20 complexes, namely $[(\text{exo-}\eta^6\text{-corannulene})Dy(\text{benzo-15-crown-5})]^{3+}$ (**1**), $[(\text{exo-}\eta^5\text{-corannulene})Dy(\text{benzo-15-crown-5})(OC(CH_3)_3)]^{2+}$ (**2**), $[(\text{exo-}\eta^5\text{-corannulene})Dy(\text{2-fluoro-benzo-15-crown-5})(OC(CH_3)_3)]^{2+}$ (**3**), $[(\text{exo-}\eta^6\text{-corannulene})Dy(\text{benzo-15-crown-5})(F)]^{2+}$ (**4**), $[(\text{exo-}\eta^6\text{-corannulene})Dy(\text{2-fluoro-benzo-15-crown-5})(F)]^{2+}$ (**5**), $[(\text{exo-}\eta^5\text{-corannulene})Dy(\text{15-crown-5})(OHCH_3)]^{3+}$ (**6**), $[(\text{exo-}\eta^5\text{-corannulene})Dy(\text{15-crown-5})(F)]^{2+}$ (**7**), $[(\text{exo-}\eta^5\text{-corannulene})Dy(\text{perfluoro-15-crown-5})(OHCH_3)]^{3+}$ (**8**), $[(\text{exo-}\eta^5\text{-corannulene})Dy(\text{perfluoro-15-crown-5})(F)]^{2+}$ (**9**), $[(\text{benzo-15-crown-5})Dy(OC(CH_3)_3)_2]^{+}$ (**10**), $[(\text{benzo-15-crown-5})Dy(Cp)_2]^{+}$ (**11**), $[(\text{benzo-15-crown-5})Dy(F)_2]^{+}$ (**12**), $[(\text{benzo-15-crown-5})Dy(Cp)(F)]^{+}$ (**13**), $[(\text{benzo-15-crown-5})Dy(OC(CH_3)_3)(F)]^{+}$ (**14**), $[(\text{benzo-15-crown-5})Dy(OCNH_2)_2]^{3+}$ (**15**), $[(\text{diaza-benzo-15-crown-5})Dy(OC(CH_3)_3)_2]^{+}$ (**16**), $[(\text{triaza-benzo-15-crown-5})Dy(OC(CH_3)_3)_2]^{+}$ (**17**), $[(\text{benzo-15-thia-crown-5})Dy(F)_2]^{+}$ (**18**), $[(\text{benzo-18-crown-6})Dy(OC(CH_3)_3)_2]^{+}$ (**19**), $[(\text{benzo-18-thia-crown-6})Dy(OC(CH_3)_3)_2]^{+}$ (**20**). Among these geometries, complexes **14** and **19** are similar to the reported X-ray structures.[11c,15] Complexes **1**−**9** constitute the corannulene-based series with equatorial corannulene ligands, whereas complexes **10**−**20** form the crown-ether-based series with equatorial crown ethers.

https://doi.org/10.1021/acs.inorgchem.5c03903
Inorg. Chem. 2025, 64, 24506−24516

2. COMPUTATIONAL DETAILS

All geometry optimizations are carried out using the Gaussian 09 suite of programs[16] at the UB3LYP functional[17] with a 6−31G* basis set[18] for H, C, O, F, N and S atoms and Stuttgart-Dresden ECPs (SDDs)[19] for Y atom. All structures were optimized by substituting Dy with Y to reduce computational cost. The ab initio calculations were performed using the MOLCAS 8.0 code. Here, we have used the following basis-set ANO···RCC VTZP for Dy and X: ANO···RCC VDZP[20] for remaining elements. The ground state f-electron configuration for Dy^{III} is $4f^9$ with $^6H_{15/2}$ multiplet as a ground state. Initial guess orbitals were generated using the GUESSORB utility, which constructs atomic-like starting orbitals suitable for multiconfigurational calculations. The generation of guess orbitals is followed by the CASSCF calculations,[21] where guess orbitals serve as starting orbitals. The CASSCF calculations have been performed with nine electrons in the seven active orbitals with an active space of CAS (9,7) for Dy^{III}. Full configuration interaction (CI) calculations were performed in this active space to achieve 21 sextet states. These 21 sextet states are spin-free states, and the RASSI module was performed to compute spin−orbit (SO) states from these states. Further, SINGLE_ANISO[22] were carried out to calculate the values of g-tensors of the low-lying eight Kramer's Doublets(KD's). Also, the anisotropy in g-factors, U_{cal} values, crystal field parameters, and direction of g_{zz} of ground KD and tunnel splitting were extracted from this set of calculations (see Tables S1 and S2).

Machine learning studies were conducted using a range of algorithms to analyze lanthanide complex data and predict magnetic properties. Our approach combined traditional regression models (linear regression, Lasso, Ridge, Elastic Net) with more sophisticated tree-based models (AdaBoost, Random Forest, gradient boosting, and extreme Gradient Boosting). For deeper insights, we implemented an artificial intelligence-driven correlation analysis using a Random Forest model with 200 decision trees, allowing unlimited depth (max_depth = None) and requiring a minimum of five samples per node split (min_samples_split = 5), with hyperparameters optimized through grid search. The analysis incorporated both raw geometric parameters (axial angle, axial−equatorial angles, Dy Displacement, Axial ratio, Equatorial angle spread and planarity index) and engineered descriptors (Symmetry Metric, Axial angle squared, Planarity symmetry and angle displacement). Performance evaluation utilized metrics including mean squared error (MSE) and R-squared (R^2) with R^2 values closer to 1 indicating better fit. All machine learning models were implemented using Python libraries such as scikit-learn, ensuring reproducibility and transparency.

3. RESULTS AND DISCUSSION

The design of high-performance Dy^{III} single-molecule magnets (SMMs) critically depends on optimizing the axial and equatorial ligand environments to enhance magnetic anisotropy and achieve higher blocking temperatures (T_B). Strong axial ligand fields are essential to stabilize the $m_J = \pm 15/2$ ground state, while weak equatorial ligation minimizes quantum tunnelling of magnetization (QTM), both of which are crucial for improved SMM performance. In this context, we have optimized 20 Dy^{III} complexes and systematically investigated their magnetic properties using SA-CASSCF/RASSI-SO/SINGLE_ANISO calculations (coordinates given in ESI). By exploring the effect of distinct crown ethers as equatorial ligands alongside strong axial ligands such as *Cp*, F^-, CH_3OH, and $(CH_3)_3O^-$, this study aims to establish a rational strategy for designing Dy^{III} -based SMMs with enhanced blocking temperatures.

3.1. Mechanism of Magnetic Relaxation in Complexes 1−9.

To systematically explore the influence of equatorial ligand fields on Dy^{III}-based SMMs, we optimized and analyzed ten corannulene-containing Dy^{III} complexes (**1**−**9**), where corannulene serves as an equatorial ligand alongside various axial donors. These systems are of particular interest as corannulene, with its curved π-system, can modulate the electron density distribution and impact the crystal field effects governing magnetization relaxation.

3.1.1. Effect of Axial Ligands on Magnetic Anisotropy. In $[(\text{exo-}\eta^6\text{-corannulene})\text{Dy(benzo-15-crown-5)}]^{3+}$ (**1**) (Figure S1a), the ground state is Ising in nature, with computed g-tensors of $g_{xx} = 0.002$, $g_{yy} = 0.020$, $g_{zz} = 19.422$ (see Table S1). The axial Dy−C bond distance is 2.475 Å, while the Dy−C(equatorial) bond distances vary from 2.362 to 2.400 Å. Due to minimal deviation in the orientation of the ground and excited state anisotropy axes, relaxation occurs from the third excited state, leading to an energy barrier (U_{cal}) of 203.2 cm^{-1} (Figure S2a). The absence of a strong axial ligand results in a moderate barrier height compared to other systems. A more axial ligand environment is introduced in $[(\text{exo-}\eta^5\text{-corannulene})\text{Dy(benzo-15-crown-5)}(OC(CH_3)_3)]^{2+}$ (**2**) (Figure 1a), where the presence of $-OC(CH_3)_3$ strengthens the axial crystal field, leading to a computed crystal field splitting energy of 650 cm^{-1} (compared to 428 cm^{-1} in **1**). The computed g-tensors remain Ising in nature ($g_{xx} = 0.002$, $g_{yy} = 0.020$, $g_{zz} = 19.422$), and relaxation occurs from the third excited state, resulting in a significantly higher U_{cal} of 365.9 cm^{-1} (Figure S2b).

Further enhancement in axiality is observed in $[(\text{exo-}\eta^5\text{-corannulene})\text{Dy(2-fluoro-benzo-15-crown-5)}(OC(CH_3)_3)]^{2+}$ (**3**) (Figure S1b), where the introduction of a fluoro-substituent in the crown ether ligand introduces a strong inductive (−I) effect that further weakens the equatorial field. This modification leads to an increased U_{cal} of 386.0 cm^{-1} (Figure S2c). The computed g-tensors indicate robust axial anisotropy ($g_{xx} = 0.002$, $g_{yy} = 0.003$, $g_{zz} = 19.934$), with relaxation occurring from the second excited state due to small QTM values. Replacing the $-OC(CH_3)_3$ ligand with a fluoride ion in $[(\text{exo-}\eta^6\text{-corannulene})\text{Dy(benzo-15-crown-5)(F)}]^{2+}$ (**4**) (Figure 1b) maintains a strong axial ligand field, albeit with a slightly lower U_{cal} (371.7 cm^{-1}, Figure S2d) compared to complex **3**. The crystal field splitting energy is lower (570.3 cm^{-1}), and despite the system adopting a more linear geometry (F−Dy−F angle = 178.9°), the relaxation still occurs from the second excited state due to a weaker axial ligand field. A similar trend is observed in $[\text{Dy(exo-}\eta^6\text{-corannulene)(F)(2-fluoro-benzo-15-crown-5)}]^{2+}$ (**5**) (Figure S1c), where fluorine substitution on the benzene ring of the equatorial ligand further reduces the equatorial field, yielding a U_{cal} of 384.5 cm^{-1} (Figure S2e).

3.1.2. Effect of Equatorial Ligand Strength on Magnetic Relaxation. The absence of benzene in the equatorial plane in $[\text{Dy(exo-}\eta^5\text{-corannulene)(15-crown-5)}(CH_3OH)]^{3+}$ (**6**) (Figure S1d) significantly alters the relaxation dynamics. The lack of an inductive effect from benzene increases the equatorial field strength, reducing the crystal field splitting energy (312.8 cm^{-1}) and lowering U_{cal} to 45.6 cm^{-1} (Figure S2f). Relaxation occurs from the first excited state, highlighting the destabilizing effect of weaker equatorial ligands. Replacing CH_3OH with fluoride in $[\text{Dy(exo-}\eta^5\text{-corannulene)(15-crown-5)(F)}]^{2+}$ (**7**) (Figure S1e)

https://doi.org/10.1021/acs.inorgchem.5c03903
Inorg. Chem. 2025, 64, 24506−24516

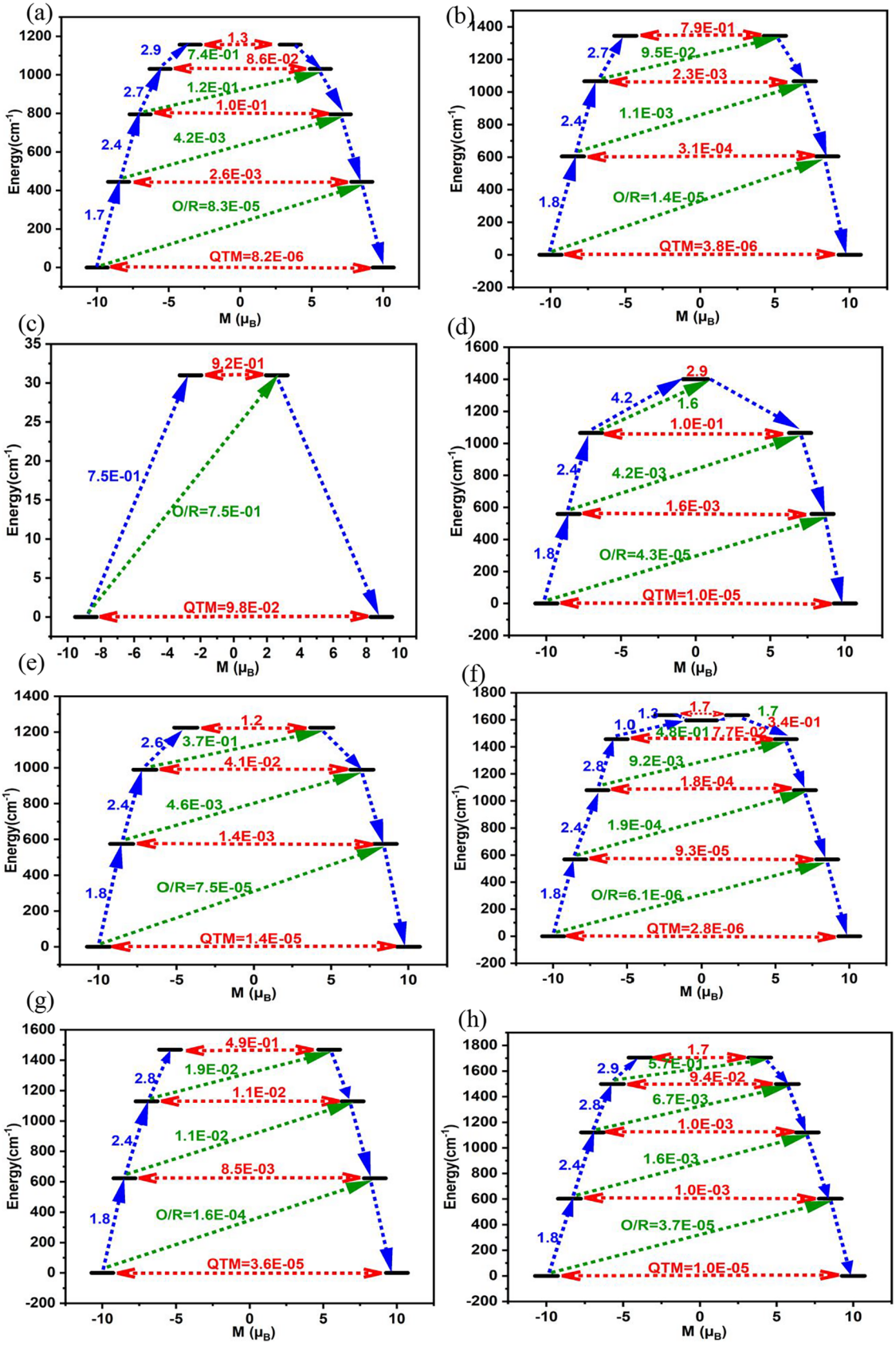

Figure 2. Ab initio computed magnetic blockade diagrams for (a) **9**, (b) **10**, (c) **11**, (d) **15**, (e) **17**, (f) **18**, (g) **19** and (h) **20**, respectively. The arrows show the connected energy states with the number representing the matrix element of the transverse moment (see text for details). The numbers above each arrow represent corresponding transverse matrix elements for the transition magnetic moments.

https://doi.org/10.1021/acs.inorgchem.5c03903
Inorg. Chem. 2025, 64, 24506−24516

Table 1. Axial Ligands, Equatorial Ligands, Energy Barriers and Remarks on the SMM Performance of 1 to 20

complex	axial ligand	equatorial ligand	equatorial bond distanes (Å)	axial bond distnaes (Å) and A1-Dy-A2 bond angle (°)	U_{cal} (cm^{-1})	notes
1	exo-η^6-corannulene	benzo-15-C-5	2.386,2.393,2.371,2.400	2.475	203.2	Relaxation occurs from the third excited state.
2	exo-η^5-corannulene, $OC(CH_3)_3$	benzo-15-crown-5	2.393,2.369,2.385,2.365,2.370	1.974,4.782 and 174.9	365.9	Enhanced axiality with $OC(CH_3)_3$.
3	exo-η^5-corannulene, $OC(CH_3)_3$	2-fluoro-benzo-15-crown-5	2.391,2.367,2.376,2.390,2.376	1.973,5.009 an 164.8	386.0	Increased barrier due to − I effect of F^- substitution on equatorial ligands
4	exo-η^6-corannulene, F^-	benzo-15-crown-5	2.403,2.370,2.331,2.391,2.352	2.042,2.743 and 178.9	371.7	Lower barrier due to F^- in place of $OC(CH_3)_3$
5	exo-η^6-corannulene, F^-	2-fluoro-benzo-15-crown-5	2.406,2.364,2.334,2.394,2.364	2.044,2.730 and 178.7	384.5	Higher barrier than **4** due to − I effect of F^- substitution on equatorial ligands
6	exo-η^5-corannulene, CH_3OH	15-crown-5	2.338,2.362,2.332,2.370,2.314	2.498,2.606 and 176.1	45.6	Low barrier and reduced crystal field splitting
7	exo-η^5-corannulene, F^-	15-crown-5	2.404,2.315,2.399,2.369,2.324	2.044,2.743 and 178.9	268.8	F^- provides a better axial ligand field than CH_3OH
8	exo-η^5-corannulene, CH_3OH	Perfluoro-15-crown-5	2.446,2.491,2.406,2.421,2.439	2.525,2.499 and 179.1	235.9	Strong − I effect on fluoro substitution of all the C atoms in the equatorial plane
9	exo-η^5-corannulene, F^-	Perfluoro-15-crown-5	2.433,2.491,2.436,2.487,2.433	2.002,2.616 and 177.4	1156.9	Enhanced axial field with F^- along with strongly enhanced − I effect
10	2 X $OC(CH_3)_3$	Benzo-15-crown-5	2.335,2.376,2.354,2.338,2.391	2.137,2.090 and 177.2	1345.5	Strong axial ligand field
11	2 X *Cp*	Benzo-15-crown-5	2.375,2.401,2.382,2.414,2.318	2.395,4.194 and 171.1	31.1	Reduced axial ligand field
12	2 X F^-	Benzo-15-crown-5	2.382,2.343,2.397,2.349,2.407	2.124,2.029 and 166.9	1346.5	Strong axial ligand field
13	F^-, *Cp*	Benzo-15-crown-5	2.396,2.453,2.401,2.475,2.433	2.119,2.427 and 178.4	913.4	Strong axial ligand field from F^-
14	F^-, $OC(CH_3)_3$	Benzo-15-crown-5	2.428,2.366,2.419,2.360,2.401	2.138,2.052 and 175.3	1471.6	High barrier due to combined axial ligands.
15	2 X $OCNH_2$	benzo-15-crown-5	2.400,2.361,2.360,2.340,2.348	3.154,2.351 and 166.3	563.2	Relaxation occurs from the fourth excited state. The axial ligands, -$OCNH_2$, do not provide as much axiality as F^- or $OC(CH_3)_3$.
16	2 X $OC(CH_3)_3$	diaza-benzo-15-crown-5	2.431,2.431,2.371,2.361,2.393	2.135,2.111 and 175.6	1224.9	Lower barrier compared to **15** due to two N in comparison to O
17	2 X $OC(CH_3)_3$	triaza-benzo-15-crown-5	2.444,2.453,2.365,2.378,2.442	2.115,2.141 and 175.4	1219.7	Similar behavior to **16**
18	2 X F^-	benzo-15-thia-crown-5	2.888,2.917,2.927,2.880,2.882	2.047,2.076 and 156.6	1634.3	Highest barrier among all complexes with a coordination number of 5 in the equatorial plane, as the Ln-S bonds are longer.
19	2 X $OC(CH_3)_3$	Benzo-18-crown-6	2.614,2.614,2.616,2.581,2.779,2.576	2.100,2.077 and 177.2	1468.9	Improved barrier compared to **18**, as Ln-O(crown ether) bonds are longer
19_{exp}	2 X $OC(CH_3)_3$	18-crown-6			1634	$[Dy(18\text{-}C\text{-}6)(OtBu)_2][I_3]$
20	$OC(CH_3)_3$ (2 ligands)	benzo-18-thia-crown-6	3.072,2.990,2.989,3.072,3.264,3.263	2.103,2.103 and 163.1	1705.0	Highest U_{cal} of all complexes, driven by favorable size and donor atoms in the equatorial plane.

https://doi.org/10.1021/acs.inorgchem.5c03903
Inorg. Chem. 2025, 64, 24506−24516

restores some axiality, increasing U_{cal} to 268.8 cm^{-1} (Figure S2g). The increased CF splitting energy (533.4 cm^{-1}) results in relaxation from the first excited state. Further increasing the −I effect in $[Dy(exo\text{-}\eta^5\text{-corannulene})(perfluoro\text{-}15\text{-}crown\text{-}5)(CH_3OH)]^{3+}$ (**8**) (Figure S 1f) introduces a perfluorinated equatorial ligand, which significantly strengthens the axial field and improves U_{cal} to 235.9 cm^{-1} (Figure 2h). The computed g-tensors remain Ising in nature (g_{xx} = 0.002, g_{yy} = 0.003, g_{zz} = 19.929), and relaxation occurs from the second excited state. A marked enhancement in axiality is observed in $[Dy(exo\text{-}\eta^5\text{-corannulene})(perfluoro\text{-}15\text{-}crown\text{-}5)(F)]^{2+}$ (**9**) (Figure 1c), where the combined effect of a fluorinated equatorial ligand and a fluoride axial ligand leads to a drastic increase in U_{cal} to 1156.9 cm^{-1} (Figure 2a). The small angles between the ground and first, second, and third excited state g_{zz} axes (0.3, 0.2, and 3.3°, respectively) contribute to relaxation from the third excited state.

3.2. Mechanism of Magnetic Relaxation in Complexes 10−20. To systematically explore the role of equatorial ligand effects on single-molecule magnet (SMM) behavior, we have optimized and analyzed 11 Dy^{III} complexes (**10**−**20**) featuring crown-ether ligands as equatorial donors and various axial ligands. The primary objective is to assess how equatorial field modulation impacts the relaxation dynamics and energy barrier (U_{cal}), which governs the blocking temperature (T_B) of these systems. Unlike the previous set of corannulene-based systems, these molecules exclusively contain crown ethers, allowing for a direct evaluation of the effects of donor atom type, ring size, and axial ligand strength.

3.2.1. Effect of Axial Ligands on Magnetic Anisotropy. In $[Dy(OC(CH_3)_3)_2(benzo\text{-}15\text{-}crown\text{-}5)]^{2+}$ (**10**) (Figure 1d), two strong-field $-OC(CH_3)_3$ ligands provide axiality, leading to a ground-state Ising nature with computed g-tensors of g_{xx} = 0.000, g_{yy} = 0.000, and g_{zz} = 19.983. The Dy−O(axial) bond lengths range from 2.091 Å to 2.137 Å, while the Dy−O(equatorial) distances vary from 2.335 to 2.391 Å. Due to the minimal deviation between the ground and excited state anisotropy axes (1.0 and 2.8° for the first and second excited states, respectively), relaxation occurs from the second excited state, yielding a substantial U_{cal} of 1345.5 cm^{-1} (Figure 2b). In $[Dy(Cp)_2(benzo\text{-}15\text{-}crown\text{-}5)]^{+}$ (**11**) (Figure S1g), replacing $-OC(CH_3)_3$ with two *Cp* ligands significantly distorts the axial ligand environment. This reduces the axial field, as reflected in the g-tensor values (g_{xx} = 0.081, g_{yy} = 0.504, g_{zz} = 17.724), and results in an increased tilt in the axial ligand coordination (*Cp*-Dy-*Cp* angle = 171.0°). Consequently, relaxation occurs from the first excited state, leading to a drastically reduced energy barrier of 31.1 cm^{-1} (Figure 2c).

A more axial ligand environment is restored in $[Dy(F)_2(benzo\text{-}15\text{-}crown\text{-}5)]^{+}$ (**12**) (Figure 1e), where two F^- ligands replace the *Cp* groups. The Dy−F bond lengths (2.124 Å to 2.029 Å) and equatorial Dy−O distances (2.349 to 2.407 Å) generate a robust axial ligand field, reflected in the g_{zz} value of 19.979. The relaxation occurs from the third excited state, leading to a U_{cal} of 1345.5 cm^{-1} (Figure 2d). Introducing mixed axial ligands in $[Dy(F)(Cp)(benzo\text{-}15\text{-}crown\text{-}5)]^{+}$ (**13**) (Figure S1h) leads to a slightly lower but still substantial axial anisotropy (g_{zz} = 19.981). The Dy−F and Dy−*Cp* bond distances (2.119 to 2.427 Å) induce small deviations in the g_{zz} axis alignment across excited states (0.0, 1.8, 3.1, and 9.9°), leading to relaxation from the fourth excited state and a U_{cal} of 913.4 cm^{-1} (Figure S2i). A further increase in axial ligand strength is seen in $[Dy(F)(OC(CH_3)_3)(benzo\text{-}15\text{-}crown\text{-}5)]^{+}$(**14**) (Figure S1i), where two of the strongest axial ligands, F^- and $-OC(CH_3)_3$, stabilize the ground-state anisotropy (g_{zz} = 19.981) and lead to relaxation from the fourth excited state with a U_{cal} of 1471.6 cm^{-1} (Figure S2j). Replacing these strong axial ligands with weaker $-OCNH_2$ ligand The Dy−N bond distances (2.361 to 2.431 Å) in $[Dy(OCNH_2)_2(benzo\text{-}15\text{-}crown\text{-}5)]^{+}$ (**15**) (Figure 1f) significantly reduces the axial field. The Dy−N(axial) bond lengths (2.351 to 3.154 Å) are longer compared to the Dy−O(axial) distances seen in earlier models, weakening the crystal field and lowering U_{cal} to 563.2 cm^{-1} (Figure S2k). The compound $[Dy(BH_4)_2(18\text{-}C\text{-}6)][Na(THF)_2(18\text{-}C\text{-}6)][BPh_4]$[11e] exhibits an effective energy barrier (U_{eff}) of 86 cm^{-1} under an applied magnetic field of 500 Oe, whereas $[Dy(18\text{-}C\text{-}6)(NO_3)_2]BPh_4$ shows a significantly lower barrier of 29.9 cm^{-1}, highlight the importance of tuning the axial ligand in obtaining superior SMMs.[11a]

3.2.2. Effect of Equatorial Ligand Donor Type. Replacing oxygen with nitrogen in the equatorial plane of $[Dy(OC(CH_3)_3)_2(diaza\text{-}benzo\text{-}15\text{-}crown\text{-}5)]^{+}$ (**16**) (Figure 1g) slightly lowers U_{cal} to 1224.9 cm^{-1} compared to its oxygen analogue (Figure S2l). The Dy−N bond distance (2.431 Å) is longer than the Dy−O bond, resulting in greater movement of the Dy ion within the equatorial plane and consequently a reduced U_{cal} value. Further in $[Dy(OC(CH_3)_3)_2(triaza\text{-}benzo\text{-}15\text{-}crown\text{-}5)]^{+}$ (**17**) (Figure S1j) maintains a comparable axial anisotropy (g_{zz} = 19.980) but results in relaxation from the fourth excited state, with a slightly reduced U_{cal} of 1219.7 cm^{-1} (Figure S2l). Substituting sulfur in the equatorial plane in $[Dy(F)_2(benzo\text{-}15\text{-}thia\text{-}crown\text{-}5)]^{+}$ (**18**) (Figure 1h) significantly enhances axiality by weakening the equatorial ligand field. The Dy−S bond distances (2.880 to 2.927 Å) are longer than the Dy−N and Dy−O counterparts, stabilizing the Ising nature up to the first excited state (g_{zz} = 19.992). Relaxation occurs from the fifth excited state, leading to a U_{cal} of 1634.3 cm^{-1} (Figure 2f). Increasing the crown ether size from 15-crown-5 to 18-crown-6 in $[Dy(OC(CH_3)_3)_2(benzo\text{-}18\text{-}crown\text{-}6)]^{+}$ (**19**) (Figure 1i) leads to Dy−O distances ranging from 2.576 to 2.779 Å, weakening the equatorial field and resulting in a higher U_{cal} of 1468.9 cm^{-1} (Figure 2g). Finally, incorporating sulfur in the expanded ring system in $[Dy(OC(CH_3)_3)_2(benzo\text{-}18\text{-}thia\text{-}crown\text{-}6)]^{+}$ (**20**) (Figure 1j) further maximizes the energy barrier, yielding the highest U_{cal} value in this study at 1705.0 cm^{-1} (Figure 2h). The Dy−S bond distances (2.989 Å to 3.264 Å) minimize equatorial interactions while maintaining strong axial anisotropy. Between the two sets of Dy^{III} SMMs studied crown ether-based systems without corannulene offer greater tunability in equatorial field modulation.

While corannulene-containing molecules generally maintain rigid equatorial environments, the crown ether systems allow for finer control of donor atom type, ligand flexibility, and steric effects. The highest U_{cal} values are consistently achieved in systems where Dy−S or D−O bond distances are maximized while retaining strong axial ligand fields. These findings reinforce the importance of weak equatorial ligand fields and strong axial ligand fields in designing high-blocking-temperature Dy^{III} magnets (see Table 1). The insights gained here provide valuable guidelines for experimental synthetic efforts in developing next-generation molecular magnets.

3.3. Correlation Analysis to Predict U_{eff} from Geometrical Parameters. Building on insights from ab initio multireference calculations, particularly CASSCF/RASSI-SO/SINGLE_ANISO, which have proven indispensable in accurately predicting the magnetic anisotropy, relaxation barriers

https://doi.org/10.1021/acs.inorgchem.5c03903
Inorg. Chem. 2025, 64, 24506−24516

Table 2. Different Geometric Descriptors along with Engineered Descriptors and Their Definitions[a]

parameters	features	formula	definition
Axial Angle	F1	$\theta_{axial} = \angle(\text{A1-Dy-A2})$	Bond angle between the two axial ligands (A1-Dy-A2)
Dy Displacement	F2	$d_{Dy} = \left\lvert z_{Dy} - \frac{1}{N}\sum_{i=1}^{N} z_{eq,i} \right\rvert$	Vertical distance of Dy from equatorial plane (Å)
Axial−Eq Angle	F3	$\theta_{axial-eq} = \frac{1}{N}\sum_{i=1}^{N} \angle(\text{Axial}-\text{Equatorial}_i)$	Average angle between axial and equatorial ligands
Axial Ratio	F4	$R_{axial} = \frac{\min(d_{A1}, d_{A2})}{\max(d_{A1}, d_{A2})}$	Ratio of shortest to longest Dy-axial bond (A1/A2)
Eq. Angle Spread	F5	$\sigma_{\theta_{eq}} = \sqrt{\frac{1}{N}\sum_{i=1}^{N} (\theta_{eq,i} - \overline{\theta_{eq}})^2}$	Standard deviation of equatorial ligand angles
Planarity Index	F6	$P = \sqrt{\frac{1}{N}\sum_{i=1}^{N} (\vec{r}_i \cdot \hat{n})^2}$	RMSD of equatorial ligands from ideal plane
Axial Angle Squared	F7	θ_{axial}^2	Captures nonlinear angular effects
Angle-Displacement	F8	Angle-Displacement $= \theta_{axial} \times d_{Dy}$	Quantifies axial geometry-displacement coupling
Symmetry Metric	F9	$S = \frac{R_{axial} \cdot \theta_{axial}}{\sigma_{\theta_{eq}}} + \epsilon,\ \epsilon = 10^{-6}$	Combines axial/equatorial symmetry into single metric
Planarity-Symmetry	F10	$P_{sym} = P \times \sigma_{\theta_{eq}}$	Links planarity with angular distribution

[a]Where θ_{axial} is the axial ligand bond angle, d_{Dy} is Dy displacement from equatorial plane, R_{axial} is axial bond length ratio, $\sigma_{\theta_{eq}}$ is equatorial angle standard deviation, P is planarity index, n̂ is the unit normal vector to equatorial plane, ϵ is the numerical stability constant, z_{Dy} is z-coordinate of Dy atom in Cartesian system, $z_{eq,i}$ is z-coordinate of the ith equatorial ligand, $\vec{r}_i$ is the position vector of ligand i relative to plane centroid.

(U_{cal}), and g-tensors of Dy^{III} -based SMMs, we turned to ML as a complementary tool for data-driven discovery. While the importance of axial ligand field strength and minimization of equatorial interactions is well-recognized, factors such as the nature and number of donor atoms, deviations from ideal geometry, and overall equatorial planarity also play critical roles in determining magnetic relaxation behavior. Here, we have systematically analyzed the Dy^{III} complexes—featuring both corannulene and crown-ether frameworks—using a set of 10 structural descriptors (F1−F10; see Tables 2 and S3) designed to encode key geometric characteristics of the molecule (see Table 2 and Scheme 2). This integrated strategy allows us not only to predict magnetic relaxation properties but also to identify which geometric features most strongly govern high-performance behavior in Dy^{III} SMMs, thereby paving the way for rational, data-guided discovery.

Scheme 2. Pictorial Representation of the Features Used in the AI/ML Calculations

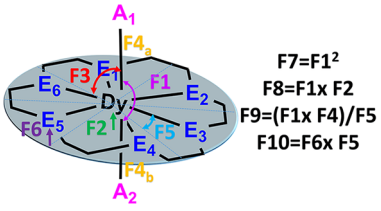

To understand how geometric distortions influence the energy barrier (U_{cal}), we performed a systematic Pearson correlation analysis[23] between key structural features and U_{cal} values (Figures 3a and S4). Among these, Dy displacement from the equatorial plane and the angular deviation from ideal axial geometry emerged as dominant factors, showing strong negative

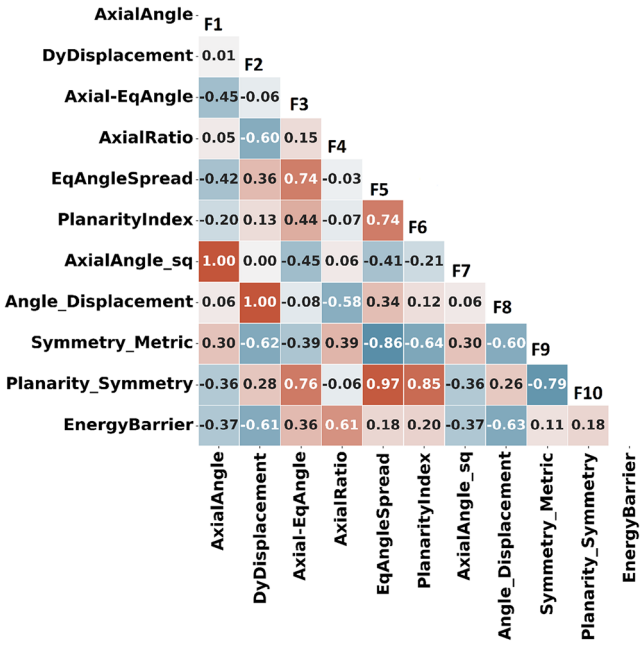

Figure 3. Ccorrelation matrix of geometric descriptors and engineered parameters for Dysprosium complexes.

correlations (−0.61 and −0.63, respectively). These distortions significantly suppress magnetic performance, as seen in complex **6**, which with a Dy displacement of 0.58 Å and angular deviation of 8.86° results in a U_{cal} > of just 45.6 cm^{-1}. In contrast, complex **18**, despite a high angular deviation (12.1°), has an extremely small Dy displacement (0.01 Å), and achieves a barrier of 1634 cm^{-1}, highlighting the greater influence of planar positioning in this case. Similarly, the axial bond angle and its squared term also

https://doi.org/10.1021/acs.inorgchem.5c03903
Inorg. Chem. 2025, 64, 24506−24516

show moderate negative correlations (−0.37), indicating that significant deviations from ideal axiality can destabilize anisotropy. For instance, complex **11**, with an axial angle of 171.1°, has a notably low U_{cal} of 31.1 cm^{-1}. On the other hand, features associated with axial symmetry exhibit positive correlations. The axial ratio, in particular, shows a strong positive relationship (+0.60) with U_{cal}. Complexes that closely approach ideal symmetry, such as complex **16** with an axial ratio of 0.99: display high barriers (1224.9 cm^{-1}), while those with more asymmetric environments, like complex **4** (axial ratio = 0.74), yield much lower values (371.7 cm^{-1}). A similar but more modest positive trend is seen with the axial−equatorial angle separation (F3), which has a correlation coefficient of +0.36. Complex **14**, for example, with F3 = 90.02°, attains a U_{cal} of 1471.6 cm^{-1}, reflecting the stabilizing role of angular isolation between axial and equatorial donor sets. Other features, such as equatorial angle spread (F5: + 0.18), planarity index (F6: + 0.20), and symmetry metrics (F9 and F10), display weaker correlations with U_{cal}, suggesting that they have relatively minor standalone effects. Notably, high-performing complexes such as complex **20** (U_{cal} = 1705 cm^{-1}), which show moderate values in these less impactful parameters, reinforce the idea that energy barrier height is predominantly governed by a small set of structurally critical factors, particularly Dy displacement, angular deviations, axial symmetry, and angular separation.

In addition to correlations with the energy barrier, the Pearson correlation matrix reveals several meaningful relationships among the structural descriptors themselves, which provide deeper insight into the geometric factors controlling magnetic anisotropy. Notably, Dy displacement (F2) shows a strong negative correlation with the axial ratio (F4: −0.60), indicating that complexes with minimal Dy displacement tend to maintain a higher axiality in their coordination environment. This relationship reinforces the idea that axial symmetry is intimately linked to the positioning of the Dy ion relative to the equatorial plane.

Similarly, equatorial angle spread (F5) exhibits a strong positive correlation with the planarity−symmetry metric (F10: +0.97), suggesting that more uniform equatorial angles promote overall planarity and symmetry in the equatorial donor set. The correlation matrix also highlights interactions between axial and equatorial features. For instance, axial−equatorial angle (F3) correlates positively with planarity−symmetry (F10: +0.76), suggesting that maintaining angular separation between axial and equatorial donors not only isolates the axial anisotropy axis but also enhances equatorial planarity. Conversely, symmetry metrics (F9) are negatively correlated with Dy displacement (F2: −0.62) and axial ratio (F4: −0.64), reinforcing that deviations in Dy positioning or loss of axiality are accompanied by a reduction in overall symmetry, which can suppress U_{cal}. Taken together, these cross-term correlations reveal that the magnetic anisotropy of Dy^{III} SMMs is governed not only by individual geometric descriptors but also by the interplay between axiality, Dy positioning, and equatorial planarity.

It is important to note that the present work focuses on establishing systematic geometric correlations with the anisotropy barrier using CASSCF calculations, thereby providing a consistent framework for comparative analysis across a diverse series of Dy(III) complexes. Previous studies have demonstrated that explicit modeling of spin−phonon coupling represents another critical step toward improving SMM performance. In particular, for selected pseudo-D_5h Dy(III) systems,[14c] it was shown how vibrational modes modulate crystal-field parameters and govern both Orbach and Raman relaxation pathways. Furthermore, a recent machine-learning (ML) model developed for D_{nh}-type molecules,[14d] capable of predicting relaxation barriers and related magnetic properties directly from structural features, offers a promising route for guiding the rational design of next-generation SMMs.

4. CONCLUSIONS

Despite significant progress in Dy^{III}-based SMMs, designing systems with high energy barriers (U_{cal} > 1000 cm^{-1}) remains a nuanced challenge due to the intricate interplay between geometric precision and ligand field modulation. This study systematically investigated a range of Dy^{III} complexes featuring crown ether and corannulene ligands, combining ab initio calculations with correlation analysis to unravel key structure−property relationships. Our findings indicate that two factors consistently limit performance: displacement of the Dy^{III} ion from the equatorial plane and angular deviation from axial symmetry. When the Dy displacement exceeds 0.25 Å and angular distortions surpass 5°, energy barriers drop sharply, typically placing such systems in the low-performance zone (U_{cal} < 500 cm^{-1}). Conversely, favorable parameters, including axial bond ratios approaching 1.0 and larger average axial−equatorial angles, are associated with improved magnetic behavior. Even when these are moderately optimized (e.g., in complex **16**), the systems often reach midlevel barrier heights (500 < U_{cal} < 1200 cm^{-1}). The best-performing complexes (e.g., **18** and **20**) exhibit axial ratios >0.90, Dy displacement <0.1 Å, and minimal angular deviation (<2°), achieving barriers in excess of 1200 cm^{-1}. While not a substitute for detailed electronic structure analysis, such models can aid in identifying patterns across chemically diverse systems, offering a valuable framework for future design efforts.

■ ASSOCIATED CONTENT

Data Availability Statement

The data supporting this article have been included as part of the Supporting Information.

Supporting Information

The Supporting Information is available free of charge at https://pubs.acs.org/doi/10.1021/acs.inorgchem.5c03903.

Optimized molecular structures, CASSCF/RASSI-SO computed anisotropy parameters, correlation matrices, additional plots illustrating geometric descriptors (F_1−F_{10}), and detailed machine-learning (ML) methodology and performance metrics (PDF)

■ AUTHOR INFORMATION

Corresponding Authors

Tanu Sharma − *Department of Chemistry, IIT Bombay, Mumbai 400076, India*; Email: tanu.sharma994@gmail.com

Gopalan Rajaraman − *Department of Chemistry, IIT Bombay, Mumbai 400076, India*; orcid.org/0000-0001-6133-3026; Email: rajaraman@chem.iitb.ac.in

Complete contact information is available at: https://pubs.acs.org/10.1021/acs.inorgchem.5c03903

Notes

The authors declare no competing financial interest.

https://doi.org/10.1021/acs.inorgchem.5c03903
Inorg. Chem. 2025, 64, 24506−24516

■ ACKNOWLEDGMENTS

GR would like to thank SERB (SB/SJF/2019-20/12; CRG/2022/001697) for funding.

■ REFERENCES

(1) (a) Aromi, G.; McInnes, E. J.; Winpenny, R. E. Recent Synthetic Results Involving Single Molecule Magnets. *Molecular Cluster Magnets* **2011**, *3*, 59−108. (b) Bartolome, S. J.; Luis, F.; Fernández, J. F. *Molecular Magnets*; Springer, 2016. (c) Caneschi, A.; Gatteschi, D.; Sessoli, R.; Barra, A. L.; Brunel, L. C.; Guillot, M. Alternating current susceptibility, high field magnetization, and millimeter band EPR evidence for a ground S= 10 state in $[Mn_{12}O_{12}(CH_3COO)_{16}(H_2O)_4].2CH_3COOH.4H_2O$. *J. Am. Chem. Soc.* **1991**, *113* (15), 5873−5874. (d) Christou, G.; Gatteschi, D.; Hendrickson, D. N.; Sessoli, R. Single-molecule magnets. *MRS Bull.* **2000**, *25* (11), 66−71. (e) Coronado, E.; Delhaès, P.; Gatteschi, D.; Miller, J. S. *Molecular Magnetism: from Molecular Assemblies to the Devices*; Springer Science & Business Media, 2013; Vol. *321*. (f) Karotsis, G.; Kennedy, S.; Teat, S. J.; Beavers, C. M.; Fowler, D. A.; Morales, J. J.; Evangelisti, M.; Dalgarno, S. J.; Brechin, E. K. $[Mn_4^{III}Ln_4^{III}]$Calix[4] arene clusters as enhanced magnetic coolers and molecular magnets. *J. Am. Chem. Soc.* **2010**, *132* (37), 12983−12990. (g) Marrows, C.; Chapon, L.; Langridge, S. Spintronics and functional materials. *Mater. Today* **2009**, *12* (7−8), 70−77. (h) Sessoli, R.; Gatteschi, D.; Caneschi, A.; Novak, M. Magnetic bistability in a metal-ion cluster. *Nature* **1993**, *365* (6442), 141−143. (i) Spaldin, N. A. *Magnetic Materials: Fundamentals and Applications*.; Cambridge University Press: 2010.

(2) Bar, A. K.; Kalita, P.; Singh, M. K.; Rajaraman, G.; Chandrasekhar, V. Low-coordinate mononuclear lanthanide complexes as molecular nanomagnets. *Coord. Chem. Rev.* **2018**, *367*, 163−216.

(3) (a) Bar, A. K.; Pichon, C.; Sutter, J.-P. Magnetic anisotropy in two- to eight-coordinated transition−metal complexes: Recent developments in molecular magnetism. *Coord. Chem. Rev.* **2016**, *308*, 346−380. (b) Feng, M.; Tong, M. L. Single ion magnets from 3d to 5f: developments and strategies. *Chem. - Eur. J.* **2018**, *24* (30), 7574−7594. (c) Goodwin, C. A.; Ortu, F.; Reta, D.; Chilton, N. F.; Mills, D. P. Molecular magnetic hysteresis at 60 K in dysprosocenium. *Nature* **2017**, *548* (7668), 439−442. (d) Guo, F. S.; Day, B. M.; Chen, Y. C.; Tong, M. L.; Mansikkamäki, A.; Layfield, R. A. A dysprosium metallocene single-molecule magnet functioning at the axial limit. *Angew. Chem.* **2017**, *129* (38), 11603−11607. (e) Guo, F.-S.; Day, B. M.; Chen, Y.-C.; Tong, M.-L.; Mansikkamäki, A.; Layfield, R. A. Magnetic hysteresis up to 80 K in a dysprosium metallocene single-molecule magnet. *Science* **2018**, *362* (6421), 1400−1403.

(4) Ungur, L.; Chibotaru, L. F. Magnetic anisotropy in the excited states of low symmetry lanthanide complexes. *Phys. Chem. Chem. Phys.* **2011**, *13* (45), 20086−20090.

(5) (a) Singh, M. K.; Yadav, N.; Rajaraman, G. Record high magnetic exchange and magnetization blockade in $Ln_2@C_{79}N$ (Ln= Gd (iii) and Dy (iii)) molecules: a theoretical perspective. *Chem. Commun.* **2015**, *51* (100), 17732−17735. (b) Singh, M. K.; Rajaraman, G. Acquiring a record barrier height for magnetization reversal in lanthanide encapsulated fullerene molecules using DFT and ab initio calculations. *Chem. Commun.* **2016**, *52* (97), 14047−14050. (c) Chen, C.-H.; Krylov, D. S.; Avdoshenko, S. M.; Liu, F.; Spree, L.; Yadav, R.; Alvertis, A.; Hozoi, L.; Nenkov, K.; Kostanyan, A.; et al. Selective arc-discharge synthesis of Dy_2S-clusterfullerenes and their isomer-dependent single molecule magnetism. *Chem. Sci.* **2017**, *8* (9), 6451−6465. (d) Liu, F.; Krylov, D. S.; Spree, L.; Avdoshenko, S. M.; Samoylova, N. A.; Rosenkranz, M.; Kostanyan, A.; Greber, T.; Wolter, A. U.; Büchner, B.; Popov, A. A. Single molecule magnet with an unpaired electron trapped between two lanthanide ions inside a fullerene. *Nat. Commun.* **2017**, *8* (1), No. 16098. (e) Velkos, G.; Krylov, D.; Kirkpatrick, K.; Liu, X.; Spree, L.; Wolter, A.; Büchner, B.; Dorn, H.; Popov, A. Giant exchange coupling and field-induced slow relaxation of magnetization in $Gd_2@C_{79}N$ with a single-electron Gd−Gd bond. *Chem. Commun.* **2018**, *54* (23), 2902−2905. (f) Velkos, G.; Yang, W.; Yao, Y.-R.; Sudarkova, S. M.; Liu, X.; Büchner, B.; Avdoshenko, S. M.; Chen, sN.; Popov, A. A. Shape-adaptive single-molecule magnetism and hysteresis up to 14 K in oxide clusterfullerenes Dy_2 O@C_{72} and $Dy_2O@C_{74}$ with fused pentagon pairs and flexible Dy−(μ_2-O)−Dy angle. *Chem. Sci.* **2020**, *11* (18), 4766−4772.

(6) Hu, Z.; Dong, B.-W.; Liu, Z.; Liu, J.-J.; Su, J.; Yu, C.; Xiong, J.; Shi, D.-E.; Wang, Y.; Wang, B.-W.; et al. Endohedral metallofullerene as molecular high spin qubit: diverse rabi cycles in $Gd_2@C_{79}N$. *J. Am. Chem. Soc.* **2018**, *140* (3), 1123−1130.

(7) Popov, A. A.; Yang, S.; Dunsch, L. Endohedral fullerenes. *Chem. Rev.* **2013**, *113* (8), 5989−6113.

(8) Nestoros, E.; Stuparu, M. C. Corannulene: a molecular bowl of carbon with multifaceted properties and diverse applications. *Chem. Commun.* **2018**, *54* (50), 6503−6519.

(9) Sharma, T.; Singh, M. K.; Gupta, R.; Khatua, M.; Rajaraman, G. In silico design to enhance the barrier height for magnetization reversal in Dy(iii) sandwich complexes by stitching them under the umbrella of corannulene. *Chem. Sci.* **2021**, *12* (34), 11506−11514.

(10) (a) Vecchi, P. A.; Alvarez, C. M.; Ellern, A.; Angelici, R. J.; Sygula, A.; Sygula, R.; Rabideau, P. W. Flattening of a curved-surface buckybowl (corannulene) by η6 coordination to $\{Cp^*Ru\}^+$. *Organometallics* **2005**, *24* (19), 4543−4552. (b) Siegel, J. S.; Baldridge, K. K.; Linden, A.; Dorta, R. d^8 Rhodium and Iridium Complexes of Corannulene. *J. Am. Chem. Soc.* **2006**, *128* (33), 10644−10645. (c) Zhu, B.; Ellern, A.; Sygula, A.; Sygula, R.; Angelici, R. J. η^6-Coordination of the Curved Carbon Surface of Corannulene ($C_{20}H_{10}$) to (η^6-arene) M^{2+} (M= Ru, Os). *Organometallics* **2007**, *26* (7), 1721−1728. (d) Filatov, A. S.; Sumner, N. J.; Spisak, S. N.; Zabula, A. V.; Rogachev, A. Y.; Petrukhina, M. A. Jahn−Teller effect in circulenes: X-ray diffraction study of coronene and corannulene radical anions. *Chem. - Eur. J.* **2012**, *18* (49), 15753−15760.

(11) (a) Ding, Y.-S.; Han, T.; Hu, Y.-Q.; Xu, M.; Yang, S.; Zheng, Y.-Z. Syntheses, structures and magnetic properties of a series of mono-and di-nuclear Dysprosium(III)-crown-ether complexes: effects of a weak ligand-field and flexible cyclic coordination modes. *Inorg. Chem. Front.* **2016**, *3* (6), 798−807. (b) Gavey, E. L.; Al Hareri, M.; Regier, J.; Carlos, L. D.; Ferreira, R. A.; Razavi, F. S.; Rawson, J. M.; Pilkington, M. Placing a crown on Dy^{III}−a dual property Ln III crown ether complex displaying optical properties and SMM behaviour. *J. Mater. Chem. C* **2015**, *3* (29), 7738−7747. (c) Xu, W. J.; Luo, Q. C.; Li, Z. H.; Zhai, Y. Q.; Zheng, Y. Z. Bis-Alkoxide Dysprosium(III) Crown Ether Complexes Exhibit Tunable Air Stability and Record Energy Barrier. *Adv. Sci.* **2024**, *11* (17), No. 2308548. (d) Wada, H.; Ooka, S.; Yamamura, T.; Kajiwara, T. Light lanthanide complexes with crown ether and its aza derivative which show slow magnetic relaxation behaviors. *Inorg. Chem.* **2017**, *56* (1), 147−155. (e) Yu, K.-X.; Ding, Y.-S.; Zhai, Y.-Q.; Han, T.; Zheng, Y.-Z. Equatorial coordination optimization for enhanced axiality of mononuclear Dy(iii) single-molecule magnets. *Dalton Trans.* **2020**, *49* (10), 3222−3227.

(12) (a) Dey, S.; Sharma, T.; Rajaraman, G. Unravelling the role of spin−vibrational coupling in designing high-performance pentagonal bipyramidal Dy(iii) single ion magnets. *Chem. Sci.* **2024**, *15* (17), 6465−6477. (b) Kragskow, J. G. C.; Mattioni, A.; Staab, J. K.; Reta, D.; Skelton, J. M.; Chilton, N. F. Spin−phonon coupling and magnetic relaxation in single-molecule magnets. *Chem. Soc. Rev.* **2023**, *52*, 4567−4585. (c) Sharma, T.; Tiwari, R. K.; Dey, S.; Mariano, L. A.; Lunghi, A.; Rajaraman, G. The mechanism of spin-phonon relaxation in endohedral metallofullerene single molecule magnets. *Chem. Sci.* **2025**, *16* (28), 13012−13021. (d) Lunghi, A.; Totti, F.; Sanvito, S.; Sessoli, R. Intra-molecular origin of the spin-phonon coupling in slow-relaxing molecular magnets. *Chem. Sci.* **2017**, *8* (9), 6051−6059.

(13) (a) Nandy, A.; Duan, C.; Kulik, H. J. Audacity of huge: overcoming challenges of data scarcity and data quality for machine learning in computational materials discovery. *Curr. Opin. Chem. Eng.* **2022**, *36*, No. 100778. (b) Editors., For chemists, the AI revolution has yet to happen *Nature* 2023; Vol. *617* 7961, p 438.

(14) (a) Golub, P.; Antalik, A.; Veis, L.; Brabec, J. Machine learning-assisted selection of active spaces for strongly correlated transition metal systems. *J. Chem. Theory Comput.* **2021**, *17* (10), 6053−6072. (b) Briganti, V.; Lunghi, A. A machine-learning framework for

https://doi.org/10.1021/acs.inorgchem.5c03903
Inorg. Chem. 2025, 64, 24506−24516

accelerating spin-lattice relaxation simulations. *npj Comput. Mater.* **2025**, *11* (1), No. 62. (c) Mondal, S.; Lunghi, A. Unraveling the Contributions to Spin−Lattice Relaxation in Kramers Single-Molecule Magnets. *J. Am. Chem. Soc.* **2022**, *144*, 22965−22975. (d) Rana, R.; Rajaraman, G. Accurate Machine Learning Predictions of Magnetization Barriers and Relaxation Times in Dnh (n = 4−6) Dy(III) Single-Molecule Magnets *Chemarxiv* DOI: 10.26434/chemrxiv-2025-h913v.

(15) Ding, Y.-S.; Blackmore, W. J.; Zhai, Y.-Q.; Giansiracusa, M. J.; Reta, D.; Vitorica-Yrezabal, I.; Winpenny, R. E.; Chilton, N. F.; Zheng, Y.-Z. Studies of the temperature dependence of the structure and magnetism of a hexagonal-bipyramidal Dysprosium(iii) single-molecule magnet. *Inorg. Chem.* **2022**, *61* (1), 227−235.

(16) Frisch, M.; Trucks, G.; Schlegel, H.; Scuseria, G.; Robb, M.; Cheeseman, J.; Scalmani, G.; Barone, V.; Mennucci, B.et al. *Gaussian 09*; Gaussian Inc.: Wallingford, CT, 2009.

(17) (a) Lee, C.; Yang, W.; Parr, R. G. Development of the Colle-Salvetti correlation-energy formula into a functional of the electron density. *Phys. Rev. B* **1988**, *37* (2), No. 785. (b) Stephens, P. J.; Devlin, F. J.; Chabalowski, C. F.; Frisch, M. J. Ab initio calculation of vibrational absorption and circular dichroism spectra using density functional force fields. *J. Phys. Chem. A* **1994**, *98* (45), 11623−11627.

(18) Hariharan, P. C.; Pople, J. A. The influence of polarization functions on molecular orbital hydrogenation energies. *Theor. Chim. Acta* **1973**, *28* (3), 213−222.

(19) Dolg, M.; Wedig, U.; Stoll, H.; Preuss, H. Energy-adjusted abinitio pseudopotentials for the first row transition elements. *J. Chem. Phys.* **1987**, *86* (2), 866−872.

(20) Roos, B. r. O.; Lindh, R.; Malmqvist, P.-Å.; Veryazov, V.; Widmark, P.-O.; Borin, A. C. New relativistic atomic natural orbital basis sets for lanthanide atoms with applications to the Ce diatom and LuF_3. *J. Phys. Chem. A* **2008**, *112* (45), 11431−11435.

(21) Malmqvist, P. k.; Roos, B. O.; Schimmelpfennig, B. The restricted active space (RAS) state interaction approach with spin−orbit coupling. *Chem. Phys. Lett.* **2002**, *357* (3−4), 230−240.

(22) Chibotaru, L. F.; Ungur, L. Ab initio calculation of anisotropic magnetic properties of complexes. I. Unique definition of pseudospin Hamiltonians and their derivation. *J. Chem. Phys.* **2012**, *137* (6), No. 064112.

(23) (a) Gravier, J.; Vignal, V.; Bissey-Breton, S.; Farre, J. The use of linear regression methods and Pearson's correlation matrix to identify mechanical−physical−chemical parameters controlling the micro-electrochemical behaviour of machined copper. *Corros. Sci.* **2008**, *50* (10), 2885−2894. (b) Nettem, C.; Rajaraman, G. How do quantum chemical descriptors shape hydrogen atom abstraction reactivity in cupric-superoxo species? A combined DFT and machine learning perspective. *Inorg. Chem. Front.* **2024**, *11* (13), 3830−3846.

https://doi.org/10.1021/acs.inorgchem.5c03903
Inorg. Chem. 2025, 64, 24506−24516